

# Diffusion-weighted MR spectroscopy of the prostate

Angeliki Stamatelidou<sup>1</sup> | Rudy Rizzo<sup>2,3,4</sup> | Kadir Simsek<sup>5,6</sup> | Jack J A van Asten<sup>1</sup> |  
Arend Heerschap<sup>1</sup> | Tom Scheenen<sup>1</sup> | Roland Kreis<sup>2,3,7</sup>

<sup>1</sup>Department of Medical Imaging,  
Radboud University Medical Center,  
Nijmegen, The Netherlands

<sup>2</sup>Magnetic Resonance Methodology,  
Institute of Diagnostic and Interventional  
Neuroradiology, University of Bern, Bern,  
Switzerland

<sup>3</sup>Translational Imaging Center,  
sitem-insel, Bern, Switzerland

<sup>4</sup>Department of Radiology, University of  
Michigan, Ann Arbor, Michigan USA

<sup>5</sup>Cardiff University Brain Research  
Imaging Centre (CUBRIC), School of  
Psychology, Cardiff University, Cardiff,  
United Kingdom

<sup>6</sup>School of Computer Science and  
Informatics, Cardiff University, Cardiff,  
United Kingdom

<sup>7</sup>Institute of Psychology, University of  
Bern, Bern, Switzerland

## Correspondence

Roland Kreis, Magnetic Resonance  
Methodology, Institute of Diagnostic and  
Interventional Neuroradiology, University  
Bern, Freiburgstr. 3, CH-3010 Bern,  
Switzerland.  
Email: [roland.kreis@unibe.ch](mailto:roland.kreis@unibe.ch)

## Funding information

HORIZON EUROPE Marie  
Skłodowska-Curie Actions, Grant/Award  
Number: 813120

## Abstract

**Purpose:** Prostate tissue has a complex microstructure, mainly composed of epithelial and stromal cells, and of extracellular (acinar-luminal) spaces. Diffusion-weighted MR spectroscopy (DW-MRS) is ideally suited to explore complex microstructure in vivo with metabolites selectively distributed in different subspaces. To date, this technique has been applied to brain and muscle. This study presents the development and pioneering utilization of <sup>1</sup>H-DW-MRS in the prostate, accompanied by in vitro studies to support interpretations of in vivo findings.

**Methods:** Nine healthy volunteers underwent a prostate MR examination (mean age, 56 years; range, 31–66). Metabolic complexation was studied in vitro using solutions with major compounds found in prostatic fluid of the lumen. DW-MRS was performed at 3 T with a non-water-suppressed single-voxel sequence with metabolite-cycling to concurrently measure metabolite and water signals. The water signal was used in postprocessing as a reference in a motion-compensation scheme. The spectra were fitted simultaneously in the spectral and diffusion-weighting dimensions. Apparent diffusion coefficients (ADCs) were derived by fitting signal decays that were assumed to be mono-exponential for metabolites and biexponential for water.

**Results:** DW-MRS of the prostate revealed relatively low ADCs for Cho and Cr compounds, aligning with their intracellular location and higher ADCs for citrate and spermine supporting their luminal origin. In vitro assessments of the ADCs of citrate and spermine demonstrated their complex formation and protein binding. Tissue concentrations of MRS-detectable metabolites were as expected for the voxel location.

**Conclusions:** This work successfully demonstrates the feasibility of <sup>1</sup>H-DW-MRS of the prostate and its potential for providing valuable microstructural information.

## KEYWORDS

diffusion MR spectroscopy, molecular complexation, MR spectroscopic imaging (MRSI), multiparametric model fitting, prostate, proton MR spectroscopy (MRS)

Angeliki Stamatelidou and Rudy Rizzo contributed equally to this work.

This is an open access article under the terms of the [Creative Commons Attribution-NonCommercial](https://creativecommons.org/licenses/by-nc/4.0/) License, which permits use, distribution and reproduction in any medium, provided the original work is properly cited and is not used for commercial purposes.

© 2024 The Authors. *Magnetic Resonance in Medicine* published by Wiley Periodicals LLC on behalf of International Society for Magnetic Resonance in Medicine.

## 1 | INTRODUCTION

Prostate tissue has a complex microstructure composed of different cell types, mainly epithelial and stromal cells, and of extracellular (acinar-luminal) spaces. Micro-structural changes involving these tissue compartments occur in common pathologies of the prostate, such as benign prostatic hyperplasia, prostatitis, and prostate cancer (PCa).<sup>1-3</sup> MRI has become a key tool in the diagnostics of PCa, typically including the measurement of multiple MRI parameters.<sup>4</sup>

An important parameter in these assessments is the apparent diffusivity of water as measured by diffusion-weighted MRI (DW-MRI), quantified by its apparent diffusion coefficient (ADC).<sup>5</sup> ADC values are affected by micro-structural features such as diffusion barriers like cell membranes, but also by the choice of acquisition parameters because the ADCs represent a weighted average value of apparent water diffusivities from multiple compartments present in each voxel. Differences in ADC values are used in clinical examinations to probe abnormal tissue morphology because of presence of cancer within the prostate.<sup>5-7</sup> As DW-MRI can operate on time-scales compatible with water molecules traversing (sub)cellular lengths, it is sensitive to tissue features at spatial scales far below the voxel size.<sup>7</sup> Therefore, going beyond conventional macroscopic assessments, various diffusion or diffusion/relaxation MRI approaches have been explored to probe microscopic tissue properties such as compartmental volume fractions, cell diameters, and cellularity.<sup>7-14</sup> However, the selectivity and specificity of these assessments depend on the compartment models used to extract these structural properties and their validation relies on correlations with histopathology of biopsies or whole mount sections that are often challenged by biased matchings with MR images.<sup>15</sup>

Besides DW-MRI, it is also possible to gauge the apparent diffusivity of tissue metabolites by diffusion-weighted <sup>1</sup>H-MR spectroscopy (DW-MRS). This technique has been applied to the brain and muscles for a more selective and specific assessment of their cellular micro-structure, assuming cell-specific presence of MRS visible metabolites.<sup>16-19</sup> Diffusion of metabolites in tissue is constrained and hindered by intra- and extra-cellular structures, fluid viscosity, and molecular interactions.

Because <sup>1</sup>H-MRS of the prostate has evolved into a mature technique to map major metabolites in this organ, it is of interest to also explore the diffusivity of these metabolites by DW-MRS as independent markers for the micro-environment of prostate tissue. Metabolites that are observed in <sup>1</sup>H-MR spectra of the prostate include citrate (Cit), total of choline-containing compounds (tCho), total

of creatine-containing compounds (tCr), polyamines with spermine (Spm) dominating this group of metabolites, and myo-inositol (mI).<sup>20</sup> Numerous studies have demonstrated that <sup>1</sup>H-MRS can distinguish between healthy and tumor tissue in the prostate and assess tumor aggressiveness.<sup>6,20</sup> An interesting aspect of prostate <sup>1</sup>H-MR spectra is that its signals arise either from metabolites located within cells such as tCho and tCr, or from the metabolites Cit, Spm, and mI that likely occur dominantly in acinar-luminal fluid.<sup>21-23</sup> Because the size of prostate cells is  $\sim 10 \mu\text{m}$ <sup>24,25</sup> and the average diameter of acinar-lumina is  $\sim 100$  to  $300 \mu\text{m}$ <sup>3,26</sup> it is expected that the diffusivity of metabolites will reflect their spatial origin.

The aim of this study was to explore DW-MRS of the prostate. Its small size and location deep inside the abdomen, surrounded by lipid tissue and pelvic muscles, necessitates accurate volume selection and lipid suppression for high quality MRS. The proximity of the bladder and mesorectum makes the organ susceptible to motion and to magnetic susceptibility differences, which is why DW-MRS is more challenging in the prostate than in brain or skeletal muscle. To address these issues, we concurrently acquired the water signal using metabolite-cycling<sup>27</sup> and implemented a motion-compensation scheme in postprocessing to correct for inter-acquisition distortions, phase and frequency fluctuations, eddy-current distortions, and nonlinear motion leading to signal loss in individual acquisitions.<sup>28,29</sup> Additionally, we dealt with the limited SNR of DW-MRS by performing simultaneous multiparametric fitting of the spectral and diffusion-attenuation dimensions.<sup>30,31</sup> Next to determining ADC values of prostate metabolites in healthy subjects, we conducted *in vitro* DW-MRS of luminal metabolites in solution to obtain reference ADCs and to support the interpretation of some *in vivo* findings. Our results demonstrate the feasibility of single voxel <sup>1</sup>H DW-MRS of the prostate and provide the first insights into the diffusivity of metabolites in this organ.

## 2 | METHODS

### 2.1 | *In vivo* study participants

For the *in vivo* study, nine healthy male subjects (mean age, 56 years; range, 31–66) were examined, who provided written informed consent to participate. Ethical approval for the measurements was obtained from Swissmedic (Bern, Switzerland) and the ethics committees of the canton Bern (Switzerland), and Radboud UMC (Netherlands).

MR data quality may be negatively affected by time-varying peristaltic activity and bladder filling. As the

common clinical contra-measures, such as anti-peristaltic drugs,<sup>20</sup> were not feasible in this volunteer study we recommended a specific diet avoiding high-fiber foods and limiting fluid consumption, respectively, 6 and 2 h prior to the MR exam.

## 2.2 | MR acquisition

All MR measurements were conducted on 3T MR systems (MAGNETOM Prisma and Prisma-Fit, Siemens Healthineers, Erlangen, Germany) with spine and body phased-array receive coils.

The MRI protocol involved  $T_2$ -weighted imaging in three orthogonal orientations using a turbo spin-echo pulse sequence with a TE of 101 ms (see Figures 1 and 2).

Single-voxel DW-MRS was performed using a non-water-suppressed STEAM pulse sequence,<sup>32</sup> optimized for diffusion measurements including a pair of diffusion-encoding pulsed field gradients with duration  $\delta$  and spacing  $\Delta$  before and after the mixing time (TM).<sup>33</sup> Metabolite-cycling was used to measure metabolite and water signals simultaneously.<sup>27,28</sup> The shortest possible TE was selected to maximize SNR, to detect short- $T_2$  metabolites and to minimize J-coupling evolution, but still

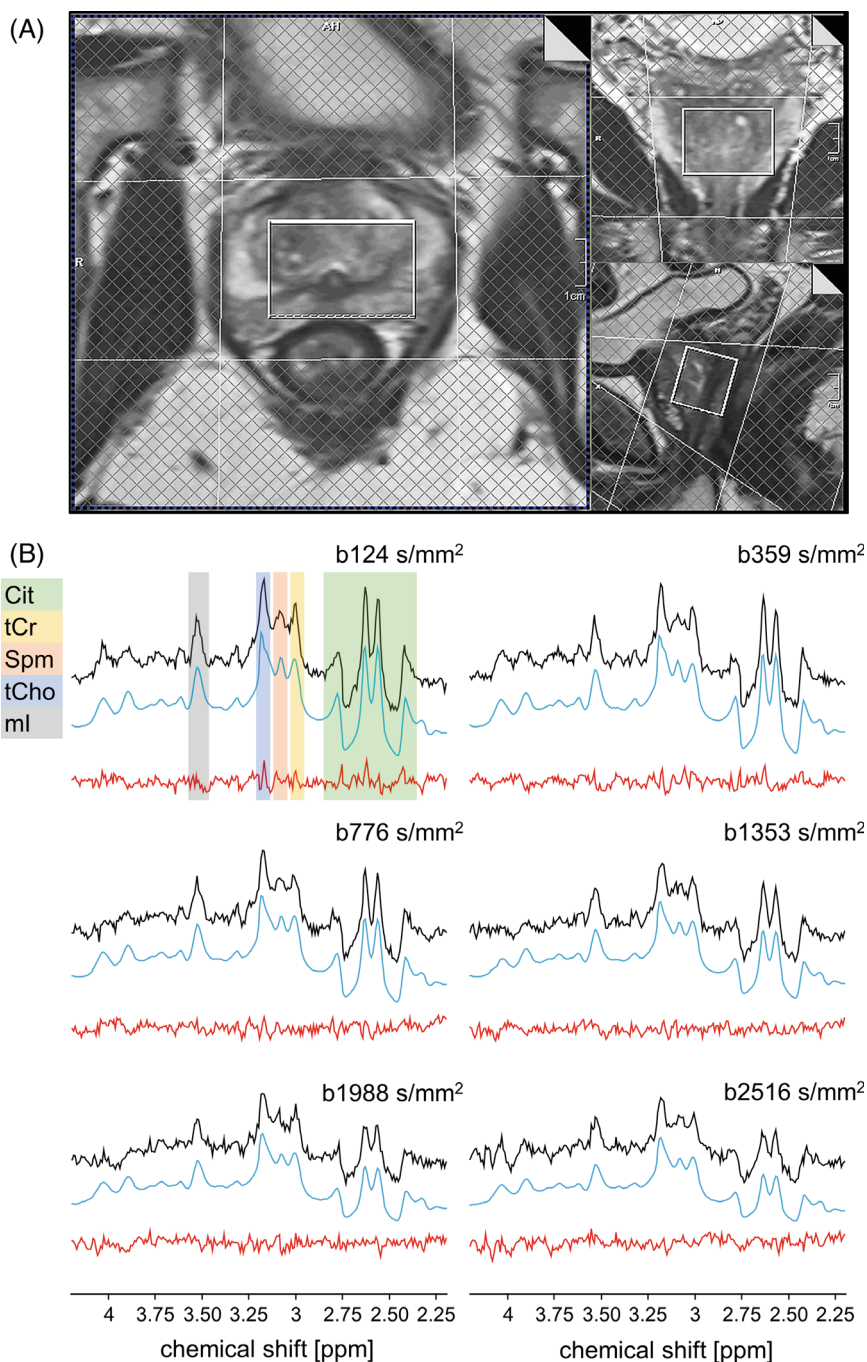


**FIGURE 1** In vivo single-voxel diffusion-weighted (DW)-MRS datasets of good quality. (A)  $T_2$ -weighted MR images showing transversal, coronal and sagittal images obtained with TR/TA of 5660/2:20, 5000/2:05, and 5590/2:20 (ms/min), respectively. FOV was  $192 \times 192 \text{ mm}^2$ . The position of the STEAM voxel (volume =  $13.2 \text{ cm}^3$ ) is indicated. (B) MR spectra acquired for six  $b$ -values. Black: experimental MR spectra after the described processing. Blue: fitted MR spectra. The base spectra used for the fit included Cit, tCho, Spm, tCr, mI, sI, Tau, and Glu. The residual traces (red) indicate excellent fits for all spectra. The signal decays clearly indicate that Cit diffuses fastest. Cit, citrate; Glu, glutamate; mI, myo-inositol; Spm, polyamines with spermine; sI, scyllo-inositol; tCho, total of choline-containing compounds; tCr, total of creatine-containing compounds; Tau, taurine; TA, acquisition time.

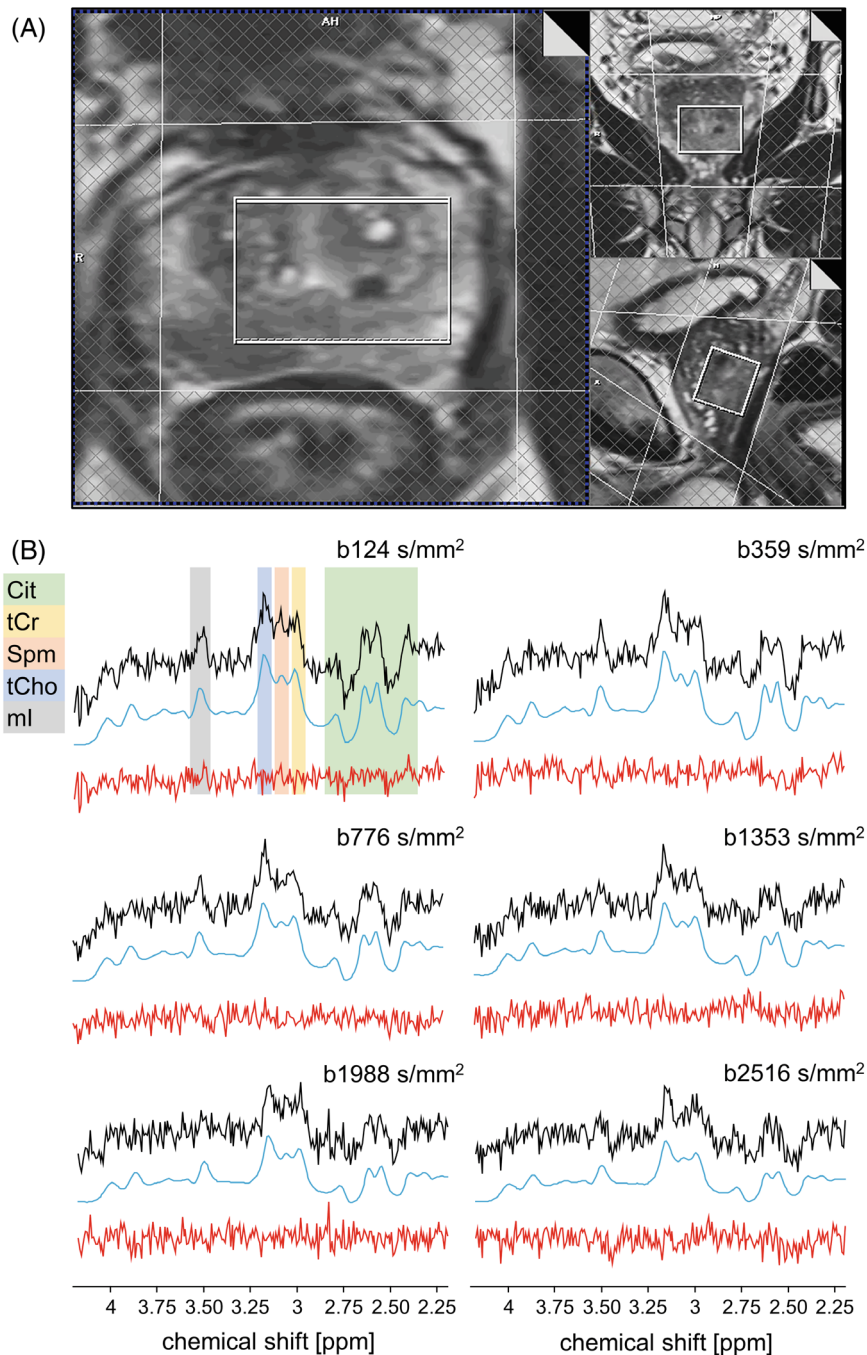


**FIGURE 2** In vivo single-voxel diffusion-weighted (DW)-MRS datasets of moderately good quality. (A)  $T_2$ -weighted MR images in the transversal, coronal, and sagittal direction showing the position of the STEAM voxel (volume =  $13.2 \text{ cm}^3$ ) (B) MR spectra acquired for six  $b$ -values. Black: experimental MR spectra after the described processing. Blue: fitted MR spectra; see Figure 1 for the included metabolite base spectra. The residual traces (red) indicate excellent fits for all spectra. Diffusion-related signal decay is clearly detected, but visual differentiation of the extent of signal decay for different metabolites is limited.

allowing sufficiently high  $b$ -values. For all scans TE was 33 ms, TM was 35 ms, and TR was 2500 ms. The applied  $b$ -values were 124, 359, 776, 1353, 1988, and 2516  $\text{s/mm}^2$  with 128 acquisitions divided into sub-spectra of 32 acquisitions. The  $b$ -value sub-spectra were recorded interleaved with readjustment of frequency or re-placement of the volume-of-interest (VOI) using interspersed MRI scans when linewidths increased.  $b$ -Values were adjusted by amplitude variation of the diffusion-sensitizing gradients with  $\delta$  and  $\Delta$  of 10 and 51.5 ms, respectively. The total acquisition time for DW-MRS was 35 minutes.

### 2.3 | Postprocessing

Postprocessing included a water-signal-based motion-compensation method in MATLAB (version 8.5.0\_R2015a; The MathWorks),<sup>28</sup> which was applied to all acquisitions of each  $b$ -value to account for signal distortions and loss caused by motion and eddy currents. Inter-acquisition distortions were corrected using the amplitude, lineshape, frequency, and phase of the water signal to adjust for phase and frequency fluctuations and eddy-current distortions and to compensate for non-linear motion.

## 2.4 | Data fitting

For simultaneous multiparametric 2D-fitting of spectra and DW signal attenuation, prior-knowledge enhanced linear combination models in FiTAID were used.<sup>30,31</sup> Base spectra were simulated of Cit, tCho (1:1 sum of glycerophosphocholine and phosphocholine), Spm, tCr (1:1 sum of Cr and phosphocreatine), mI, scyllo-inositol (sI), taurine (Tau) and glutamate (Glu) using VeSPA,<sup>34</sup> assuming ideal RF pulses. The fits of the latter three metabolites resulted in small, very variable intensities and are not reported. Chemical shifts and J-couplings for Cit and Spm were adapted to best match the observed spectral patterns. Resonances were fitted between 2.3 and 4.2 ppm and modeled with Voigt lineshapes assuming that the Gaussian damping represents field inhomogeneity and the Lorentzian damping  $T_2$  relaxation. Gaussian broadening was identical across metabolite signals, but variable over different  $b$  values, and Lorentzian broadening was different across metabolite signals, but homogenous across  $b$  values. Starting values for Lorentzian broadenings were drawn from published  $T_2$  values.<sup>35–38</sup> Three broad Voigt baseline components were added, centered at 1.4, 2.1, and 3.85 ppm, to accommodate lipid signal contamination in the 1 to 2 ppm range and water residuals and unknown baseline components at 3.6 to 4 ppm. Signal amplitudes were restricted to positive values. Linewidths were derived from the real part of the spectra. Phase and frequency offsets were modeled as a single identical variable each across all metabolites. The frequency offset was left to vary across  $b$  values.

The 2D fit model was optimized on a high-SNR cohort-average spectrum, which was constructed after signal alignment and relative normalization by scaling with the corresponding water signal. Fitting errors were estimated as Cramer-Rao lower bounds (CRLBs).

The signal decay along the second dimension was modeled as a mono-exponential function:

$$S(b) = S_0 e^{-b \text{ADC}}, \quad (1)$$

where  $S(b)$  is the amplitude of the respective metabolite base spectrum in the linear combination model at a specific  $b$  value,  $S_0$  the amplitude without diffusion-weighting, and ADC.

Attenuation of the water signal was represented by a biexponential decay, separating a fast and a slow diffusing component:

$$S^w(b) = S_{0s}^w e^{-b \text{ADC}_s} + S_{0f}^w e^{-b \text{ADC}_f}, \quad (2)$$

$$S_0^w = S_{0s}^w + S_{0f}^w. \quad (3)$$

$\text{ADC}_s$  and  $\text{ADC}_f$  are the ADCs of the slow and fast diffusing water entities, respectively.  $S_{0s}^w$  and  $S_{0f}^w$  are their respective amplitudes without diffusion-weighting.

$$f_s = \frac{S_{0s}^w}{S_0^w}, \quad (4)$$

$$f_f = \frac{S_{0f}^w}{S_0^w}, \quad (5)$$

$f_s$  and  $f_f$  are the signal fractions of slow and fast diffusing water moieties, respectively.<sup>39,40</sup>

## 2.5 | Absolute quantification

For absolute quantification of metabolite tissue contents,  $[C_{\text{met}}]$ , the metabolite signals ( $S_0^{\text{met}}$ ) were referenced to the total water signal  $S_0^w$ .<sup>41</sup> Signal attenuation due to  $T_1$  and  $T_2$  relaxation for metabolites ( $\text{ATT}_{T_{1,\text{met}}}$ ,  $\text{ATT}_{T_{2,\text{met}}}$ ) and water ( $\text{ATT}_{T_{1,w}}$ ,  $\text{ATT}_{T_{2,w}}$ ) were estimated using literature values<sup>42</sup> and for water as tissue average without specification to different prostate compartments. The  $T_1$  and  $T_2$  values used for the metabolite signals were: Cit<sup>35</sup>: 0.47 s and 0.17 s; tCho<sup>35</sup>: 1.1 s and 0.22 s; tCr<sup>36</sup>: 1.13 s and 0.19 s; Spm: 0.708 s<sup>43</sup> and 0.096 s<sup>37</sup>; mI: 1.0 s and 0.09 s,<sup>38</sup> respectively. For water, the used overall  $T_1$  and  $T_2$  were 1.60 s and 0.14 s, respectively, as determined for peripheral zone (PZ).<sup>44–46</sup> The tissue metabolite concentrations were calculated assuming an overall MR-detectable water content of 40.2 M ( $[C_{\text{tissue-w}}]$ ), as derived from 39.4 mol/kg wet weight,<sup>47</sup> and a prostate tissue density of 1.02 kg/L.<sup>48</sup> The number of protons per metabolite is automatically considered in the basis signals

$$[C_{\text{met}}] = \left( \frac{S_0^{\text{met}}}{S_0^w} \right) \left( \frac{\text{ATT}_{T_{1,w}} \text{ATT}_{T_{2,w}}}{\text{ATT}_{T_{1,\text{met}}} \text{ATT}_{T_{2,\text{met}}}} \right) [C_{\text{tissue-w}}]. \quad (6)$$

## 2.6 | In vitro study

To investigate the effects of potential molecular interactions on ADCs of metabolites in lumen, DW-MRS was conducted on 6 solutions with compounds occurring in expressed prostatic fluid (EPF),<sup>21–23,49</sup> assuming this represents luminal fluid (see Table 1).

Solutions 1 to 4 were prepared to investigate interactions between individual metabolites in the presence of metal ions. Solution 5 mimics the composition of human EPF including bovine serum albumin (BSA) as protein surrogate<sup>50</sup> and solution 6 was included to examine the effect of higher protein levels.

TABLE 1 Chemical composition of solutions for the in vitro study.

	Solution 1	Solution 2	Solution 3	Solution 4	Solution 5	Solution 6
Cit [mM]	–	90	90	18	90	90
Spm [mM]	18	–	18	79	18	18
mI [mM]	6	6	6	6	6	6
CaCl <sub>2</sub> 2H <sub>2</sub> O [mM]	18	18	18	18	18	18
MgCl <sub>2</sub> [mM]	15	15	15	15	15	15
KCl [mM]	61	61	61	61	61	61
ZnCl <sub>2</sub> [mM]	9	9	9	9	9	9
BSA (g)	–	–	–	–	15	50

Note: Solutions were prepared in 300 mL spherical glass flasks in Milli-Q water and adjusted to pH = 7.1 ± 0.05 using NaOH and HCl solutions. After 24 hours to allow for equilibrium-formation, they were stored at 4°C. Chemicals were procured from Sigma-Aldrich.

Abbreviations: BSA, bovine serum albumin; Cit, tri-sodium citrate dihydrate; mI, myo-inositol; Spm, spermine tetrahydrochloride.

The DW-MRS acquisition protocol was identical to the in vivo study, but with different *b*-values (124, 359, 776, 1353, 1988, 2516, 3106, 3759 s/mm<sup>2</sup>), 16 averages and a VOI of 64.0 cm<sup>3</sup>. All MR measurements were performed at 37.0°C ± 0.5°C.

Postprocessing was as for the in vivo data, but without motion-compensation and a fitting range of 1.1–4.3 ppm. The basis set involved the metabolites Cit, Spm, and mI, with a singlet at ~1.9 ppm to fit a small signal appearing with BSA addition. The spectral basis patterns for Spm and Cit were extracted from the lowest *b*-value spectrum for each solution rather than from simulations to account for changes in spectroscopic patterns because of variations of their spin system configuration caused by the specific composition of the solution.

## 2.7 | Expression of results and statistics

Metabolite ADCs and tissue contents describing the cohort were derived in two ways. First, they were determined as a weighted average over the estimated values from all subjects, with the weights defined by the normalized inverse CRLB for each estimated parameter. These results are accompanied by weighted-cohort SDs (same weights). They are referred to as weighted average (w-avg) ± w-SD. Second, alternative group results were derived as estimated parameters from a cohort-averaged dataset that had been created by averaging spectra from all subjects and for all *b*-values (rather than by averaging fitting results as indicated before). Here, the uncertainty is indicated by the CRLBs of this single fit. These results are referred to as averaged spectra (avg-spec) ± CRLB. For statistical analyses, OriginPro 2019b (OriginLab Corporation) was used. To investigate potential differences in metabolite diffusivities, a repeated-measures analysis of variance

(ANOVA) was conducted (without weights). Bonferroni post hoc pairwise comparison was performed to determine which metabolite diffusivities deviate significantly from the others. The level of significance was set to 0.05 for all tests.

## 3 | RESULTS

### 3.1 | In vivo data quality

The prostates of the nine healthy subjects differed substantially in volume. The STEAM-localized VOI placed within the prostate (mean size, 13.9 cm<sup>3</sup>) covered ~60% of the central gland (transition zone [TZ] and central zone [CZ]) and ~40% of PZ tissue, but the actual central gland/PZ ratio per VOI was different for each subject. Magnetic field homogeneity within the VOI varied between subjects, likely because of anatomical and volume variations and air-tissue susceptibility differences. The Gaussian linewidth of the water signal over the cohort of the nine subjects was 5.5 ± 2.9 Hz (range, 2.4–12.4 Hz), as averaged from all measured *b*-value spectra for each subject. SNR also varied prominently in this cohort with a time-domain water SNR averaged over all *b*-values of 2.72 ± 0.95 × 10<sup>3</sup>. In the STEAM spectra (Figures 1 and 2), distinct signals were observed for Cit (2.6 ppm), tCr (3.0, 3.9 ppm), Spm (1.8, 2.1, 3.1 ppm), tCho (3.2, 3.5, 4.0 ppm), and mI (3.5 ppm). With narrow linewidths and adequate SNR, these signals were discernable across all measured *b*-values (Figure 1). Metabolite signals with larger linewidths and/or lower SNR were not always visible and/or well-resolved for every *b*-value (Figure 2).

Simultaneous 2D fitting resulted in flat residuals across all *b*-values, both for excellent and moderate quality

spectra (Figures 1 and 2). The cohort-average spectra visualize best the diffusion-related signal decay for all observable prostate metabolites and the decomposition into the spectral contributions of each of these metabolites (Figure 3).

### 3.2 | In vivo ADCs and tissue concentrations

Visual inspection of the cohort-averaged spectra (avg-spec) reveals that the Cit signal decays fastest among all metabolite signals (Figure 3). A relatively high ADC for Cit follows from a quantitative evaluation, both from the w-avg of the single-subject estimates and from fitting the cohort avg-spec (Table 2). In both approaches, the ADC of Cit was significantly higher than ADCs of the other metabolites ( $p < 0.05$ ). The ADC values for tCho and tCr had the lowest

w-avg values of all metabolites (Table 2). The ADC of mI was in the same range for the avg-spec, but was intermediate between these and the ADC of Cit for the w-avg values. In both evaluations, the ADC of Spm had an intermediate value between those of Cit and tCho or tCr.

Uncertainties of the estimated ADC values can be derived from the variance over the cohort, the CRLBs for the avg-spec data set (Table 2), as well as the average and range of CRLB values for individual subject data (Table 3). Except for tCho, the SDs over the cohort were at least two times larger than the mean CRLB found for the individual estimates indicating substantial inter-subject differences or further sources of variance that are not reflected in the CRLBs. The six to 15-fold CRLB difference between the best and worst dataset (minimum vs. maximum) reflects the large inter-subject difference in data quality, which is likely because of different SNR (VOI size, coil loading) and field homogeneity. The small CRLBs

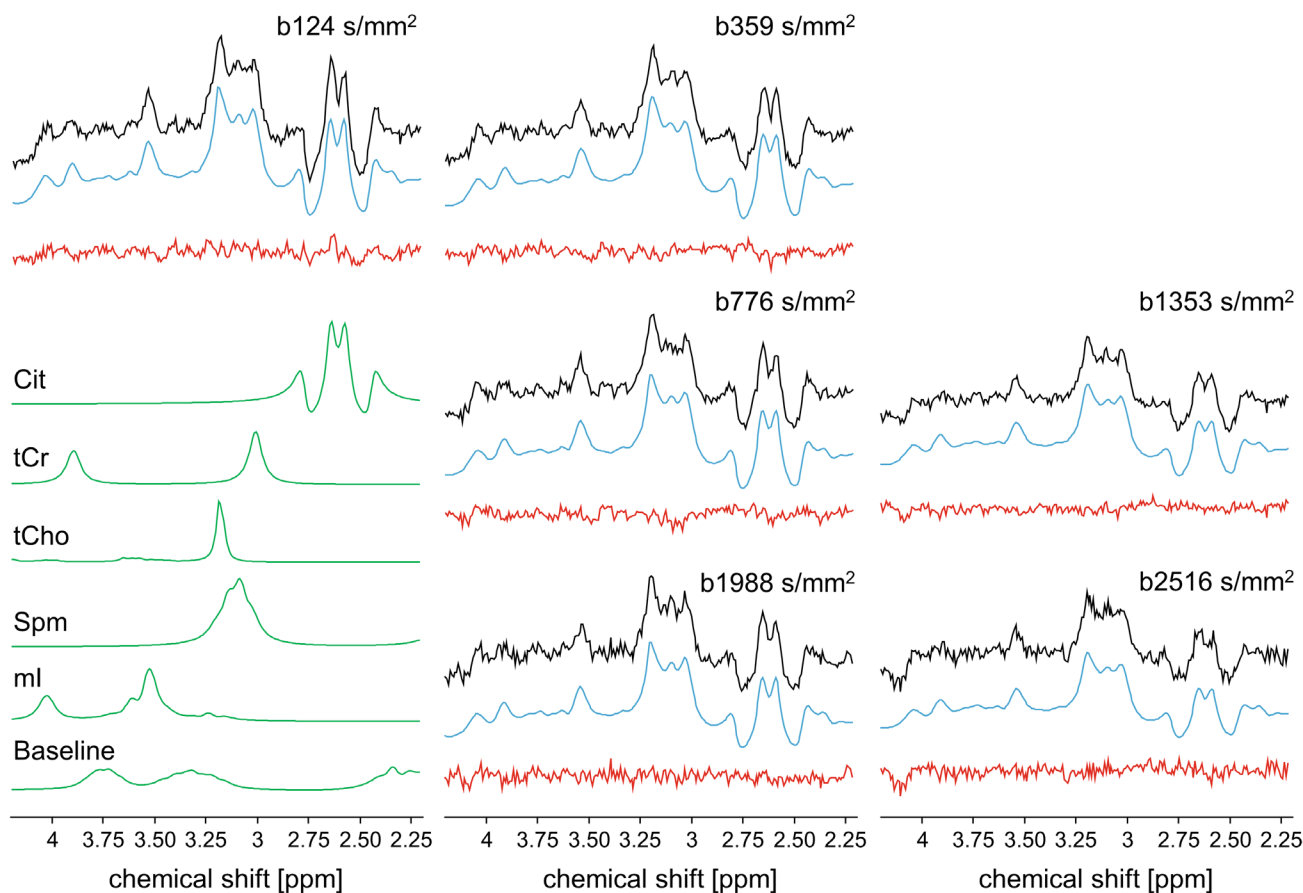


**FIGURE 3** In vivo single-voxel diffusion-weighted (DW)-MRS of cohort-averaged spectra (avg-spec) obtained from nine volunteers. The fitted spectra (in blue) represent the experimental data (in black) well, but SNR in the avg-spec case is much better than in the individual data, such that limits in the spectral model become visible in the form of non-random residuals. In these optimal SNR data the metabolite patterns, also for low-concentration metabolites, are well delineated, in particular the presence and diffusion dependence of the full mI spectrum and the methylene peak of tCr can be well discerned. Estimated individual and separated metabolite contributions to the lowest  $b$ -value spectrum are plotted in the lower left corner of the Figure. The base spectra are described in Figure 1. Fit residuals are plotted in red. Cit, citrate; mI, myo-inositol; Spm, polyamines with spermine; tCho, total of choline-containing compounds; tCr, total of creatine-containing compounds.

TABLE 2 Apparent diffusion coefficients (ADCs) and tissue concentrations of prostate metabolites estimated by in vivo DW-MRS.

	w-avg ADC $\pm$ w-SD [ $\times 10^{-4}$ mm <sup>2</sup> /s]	avg-spec ADC $\pm$ CRLB [ $\times 10^{-4}$ mm <sup>2</sup> /s]	w-avg abs conc $\pm$ SD [mM]	avg-spec abs conc $\pm$ CRLB [mM]
Cit	2.86 $\pm$ 0.51	2.48 $\pm$ 0.07	22.7 $\pm$ 11.6	28.73 $\pm$ 0.53
Spm	1.59 $\pm$ 0.54	1.80 $\pm$ 0.06	10.5 $\pm$ 5.7	11.98 $\pm$ 0.17
mI	1.52 $\pm$ 0.22	1.41 $\pm$ 0.09	18.6 $\pm$ 5.3	22.44 $\pm$ 0.41
tCho	1.47 $\pm$ 0.45	1.64 $\pm$ 0.13	2.86 $\pm$ 0.65	2.86 $\pm$ 0.34
tCr	1.19 $\pm$ 0.56	1.34 $\pm$ 0.09	4.02 $\pm$ 0.98	4.77 $\pm$ 0.12
Water	ADC <sub>s</sub> : 4.8 $\pm$ 1.1/ <i>f<sub>s</sub></i> : 62 $\pm$ 8% ADC <sub>f</sub> : 22.9 $\pm$ 5.2/ <i>f<sub>f</sub></i> : 38 $\pm$ 8%	ADC <sub>s</sub> : 5.51/ <i>f<sub>s</sub></i> : 69% ADC <sub>f</sub> : 30.00/ <i>f<sub>f</sub></i> : 31%		

Note: ADCs are given as estimate from a weighted average (w-avg) of individual subjects' results and as estimated from the fitted spectrum obtained from the full cohort of healthy volunteers avg-spec. Additionally, the w-avg absolute concentration values from the individual subjects' results (w-avg abs conc), and the absolute concentration estimated from the fitted spectrum obtained after averaging the full cohort of the healthy volunteers (avg-spec abs conc) are presented. Abbreviations: abs, absolute; ADC<sub>f</sub>, fast diffusion entity; ADC<sub>s</sub>, slow diffusion entity; avg-spec, averaged spectrum; Cit, citrate; conc, concentration; CRLB, Cramer-Rao lower bound; *f<sub>f</sub>*, signal fraction of fast diffusing component; *f<sub>s</sub>*, signal fraction of slow diffusing component; mI, myo-inositol; Spm, polyamines with spermine; tCho, total of choline-containing compounds; tCr, total of creatine-containing compounds; w-avg, weighted average.

TABLE 3 Estimated CRLB values for the metabolite ADCs.

[ $\times 10^{-4}$ mm <sup>2</sup> /s]	CRLB avg	CRLB min	CRLB max
Cit	0.2	0.06	0.64
Spm	0.23	0.05	0.73
mI	0.28	0.09	0.54
tCho	0.38	0.12	0.73
tCr	0.32	0.12	0.75

Note: Average, minimal and maximal CRLB values from the individual subject data are given in absolute units. Abbreviations: avg, average; Cit, citrate; CRLB, Cramer-Rao lower bound; max, maximum; mI, myo-inositol; min, minimum; Spm, polyamines with spermine; tCho, total of choline-containing compounds; tCr, total of creatine-containing compounds.

obtained for the ADCs of all metabolites from the avg-spec dataset ( $0.06 \times 10^{-4}$  mm<sup>2</sup>/s to  $0.13 \times 10^{-4}$  mm<sup>2</sup>/s) indicate that the model-related uncertainty is very small if the SNR is high.

The biexponential fit of the water signal decay provided two distinct ADC values (difference by a factor of at least 4, see Table 2). The volume fraction of the high ADC component was  $38\% \pm 8\%$  and that of the low component  $62\% \pm 8\%$ .

Table 2 also lists estimated tissue metabolite concentrations. The w-avg tissue contents tend to be somewhat lower than the avg-spec estimates. The cohort SDs are mostly substantially higher than the CRLBs from individual spectra (which are  $\sim 3$  times larger than the CRLB from the avg-spec), indicating substantial concentration differences between subjects, in particular for Cit and Spm (but not tCho), potentially because of variable contents in the VOIs of TZ and PZ tissue.

### 3.3 | In vitro results

The good SNR and small linewidths of solution spectra allowed measurements up to *b*-values of 3759 s/mm<sup>2</sup> despite fast diffusion of water-dissolved metabolites. Figure 4 presents DW spectra acquired from solution 5 with metabolite concentrations in the range observed for prostatic fluids.<sup>21–23,49</sup> Estimated ADCs of all metabolites in all solutions were substantially larger in vitro than for these metabolites in vivo; both measured at  $\sim 37^\circ\text{C}$  (Table 4).

Changes in relative concentrations of Cit and Spm significantly affected the ADCs of both metabolites. Adding Cit to a Cit-free solution of Spm in a 5:1 ratio (solutions 3 vs. 1) led to slower diffusion of Spm with a reduction of 22% for its ADC. Inversely, adding Spm to a Spm-free solution of Cit (solutions 3 vs. 2) in a 1:5 ratio led to slower diffusion of Cit with a reduction of 7% for its ADC, and increasing Spm content to a 4:1 ratio (solution 4 vs. 3) reduced Cit diffusion further with an additional decrease in ADC of 16%.

BSA in the media differently affected metabolite diffusion. By adding 15 g/L BSA the ADC of Cit and Spm reduced by  $\sim 10\%$  (solution 5 vs. 3), whereas the effect was more pronounced for mI with an ADC reduction of  $\sim 25\%$ . Increasing BSA to 50 g/L (solution 6) did not affect the ADC values of Cit and Spm, but further reduced the ADC of mI by  $\sim 23\%$  (compared to solution 5).

Mono-exponential water ADCs were found to be  $\sim 29 \times 10^{-4}$  mm<sup>2</sup>/s (solutions 1–4), which is slightly below the value expected for free diffusion at  $37^\circ\text{C}$  ( $30 \times 10^{-4}$  mm<sup>2</sup>/s).<sup>51</sup> This ADC seemed most affected by the addition of BSA (solutions 5 and 6).



**FIGURE 4** In vitro single-voxel diffusion-weighted (DW)-MRS dataset. MR spectra acquired for eight  $b$ -values of solution 5 that approaches realistic concentrations of molecules in luminal fluid. Black: experimental spectra after the described processing; Blue: fitted spectra; Red: fit residual.

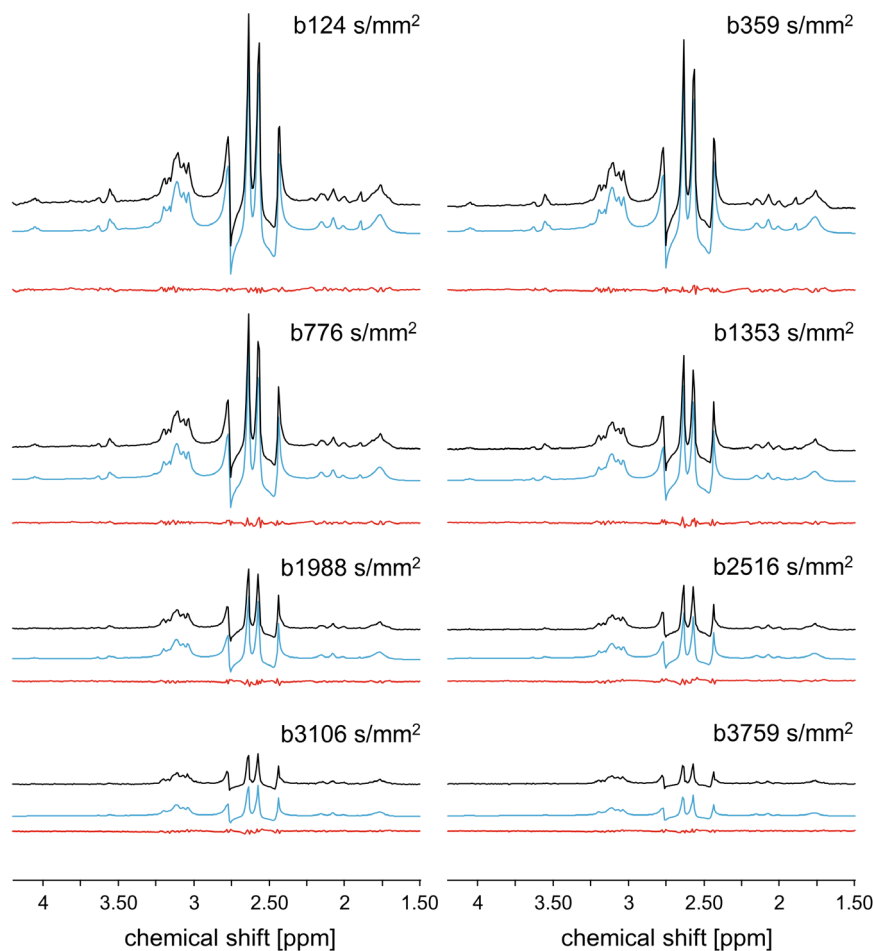


**TABLE 4** Estimated ADC values of metabolites and water from the in vitro study at 37°C.

$[\times 10^{-4} \text{ mm}^2/\text{s}]$ (CRLB <2%)	Solution 1	Solution 2	Solution 3	Solution 4	Solution 5	Solution 6
Cit		7.3	6.8	5.7	6.0	6.1
Spm	7.2		5.6	6.4	5.0	5.0
mI	10.7	9.5	11.1	13.7	8.3	6.4
H <sub>2</sub> O	29.9	28.9	28.5	29.3	28.1	27.9

Abbreviations: Cit, citrate; CRLB, Cramer-Rao lower bound; mI, myo-inositol; Spm, polyamines with spermine.

## 4 | DISCUSSION

Diffusion-weighted-MRS emerges as a highly suitable tool for the in vivo exploration of intricate microstructures, facilitated by the cell- or compartment-specific presence of different metabolites. The technique offers a noninvasive window on molecular displacements occurring over scales comparable to and below cell dimensions. Data interpretation can be challenging in biological tissues, in which not only viscosity and physical hindrance by cellular boundaries play a role, but also exchange across boundaries and complexation of metabolites. Nevertheless, detection of differences in metabolite diffusivity can stand as an

effective strategy to elucidate micro-environmental features.<sup>19,52</sup>

In this work, the application of <sup>1</sup>H-DW-MRS was extended for the first time to the prostate, using dedicated acquisition and postprocessing techniques, resulting in successful estimations of the in vivo diffusivity of Cit, tCho, tCr, mI, Spm, and water. Although 3D-MRSI is the standard localization method in prostate MRS, the currently used sequences were considered to have too long minimal acquisition times. Therefore, we chose single voxel localization with non-water-suppressed STEAM for this pioneering venture. Moreover, relatively large VOIs were selected to obtain adequate SNR. This approach allowed a

short TE, enabling to include mI, a metabolite challenging to detect with standard 3D  $^1\text{H}$ -MRSI of the prostate. The anatomical position of the prostate within the lower abdomen is challenging for DW-MRS because of motion and changes in local susceptibility induced by continuous bladder filling and intermittent movement of bowel content (including changes in location and size of air spaces). This caused suboptimal shimming and diminished SNR, which we addressed in postprocessing with a scheme to correct motion-induced signal distortions and with 2D fitting for consistent signal estimation over the whole dataset.<sup>28,31</sup> Our approach also allowed estimation of metabolite tissue content using the water signal as internal reference. Interpretation of the in vivo diffusion data was supported by an in vitro study of solutions with various metabolite compositions.

#### 4.1 | Microenvironments in the prostate

Prostate tissue is mainly composed of epithelial cells and stroma (smooth muscle cells and connective tissue including extracellular matrix), as well as of extracellular (acinar-luminal) spaces.<sup>3,53,54</sup> This constitutes a complex microenvironment with dissimilar local metabolite concentrations and vastly different surroundings for water and metabolite diffusion. The relative volume fractions of these components vary within and between central gland (TZ and CZ) and PZ, leave alone the changes that come with pathology.<sup>1,55</sup> Luminal area or volume fractions in normal prostate PZ tissue, estimated by segmentation of histopathological specimens, are  $\sim 25\%$  with reported average values between  $\sim 20$  and  $\sim 30\%$ .<sup>9,12,13,56–61</sup> Luminal volume fractions derived from models applied to DWI and  $T_2$  data of water are usually higher (average values,  $\sim 30\%$ – $40\%$ ), depending on the models applied.<sup>9,12,13,59</sup> Variations in luminal volume fraction also occur across regions: it is often somewhat lower for the TZ<sup>9,12,13,61</sup> and much lower close to the urethra and at the anterior fibromuscular stroma,<sup>9,58</sup> and variable for pathologies (e.g., higher in glandular BPH<sup>62</sup> and significantly lower in PCa).<sup>9,12,13,56–58,60</sup>

As further argued below, Cit and Spm and probably also mI primarily reside in the luminal space while tCho and tCr occur intracellularly, in principle in all cell types. It is anticipated that molecular diffusion is least restricted in lumen and most hindered in cells.

Although the prostate water signal attenuation by diffusion-weighting with extended  $b$ -values can be represented as a biexponential decay, it is not straightforward that the fast decaying component could be assigned to luminal and the slow component to intracellular water.<sup>63,64</sup> Microscopic diffusion studies of formalin-fixed

prostate tissue have identified at least three compartments with significantly different water diffusivity: a ductal high diffusivity, an epithelial low diffusivity, and an intermediate diffusivity for the stromal compartment.<sup>8,65</sup> Stromal tissue comprises heterogeneous environments including extracellular space and smooth muscle cells that are expected to feature faster water diffusion than observed for other cell types, but still slower than for large luminal spaces. Hence, the relative contribution of signal from this environment to either fast or slow decaying components will depend on multiple factors, including physiological factors such as water exchange between the different compartments as well as technical factors of the diffusion-weighting pulse sequence used (number and size of  $b$ -values, diffusion time, diffusion encoding scheme).

#### 4.2 | Metabolite and water diffusion

To our knowledge, no ADC values have been reported for prostate metabolites. Literature values are available for the brain and skeletal muscle,<sup>16–18</sup> with tCho and tCr (as well as mI in brain) as common metabolites. Their ADC values ( $1.3$ – $1.6 \times 10^{-4}$  mm<sup>2</sup>/s), which are lowest among all metabolites in this work, confirm their expected intracellular origin. Compared to other organs the diffusion of these metabolites is in the same ballpark as in brain gray matter for similar diffusion times ( $1.3$ – $1.5 \times 10^{-4}$  mm<sup>2</sup>/s),<sup>66–68</sup> but substantially slower than in skeletal muscle tissue at much longer diffusion time ( $6$ – $7 \times 10^{-4}$  mm<sup>2</sup>/s parallel;  $3$ – $4 \times 10^{-4}$  mm<sup>2</sup>/s orthogonal to muscle fibers).<sup>18</sup> Given the dominating luminal contribution to the in vivo signals of Cit and Spm and knowing that the average luminal diameter is much bigger than the size of epithelial and stromal cells, one expects their ADCs to be clearly larger than the ADCs of cellular metabolites. Our findings indeed support this expectation, with the ADC for Cit being nearly double that of tCr and tCho. However, for Spm, this difference is smaller, possibly because of complexation (vide infra).

The water signal diffusion decay showed a clear biexponential behavior in agreement with other DWI studies that included high  $b$ -values.<sup>63,64</sup> Both the fast ADC component, estimated at  $22.9 \pm 5.3 \times 10^{-4}$  mm<sup>2</sup>/s, and the slow component at  $4.8 \pm 1.1 \times 10^{-4}$  mm<sup>2</sup>/s are comparable to ADC values of these components reported by others applying DWI to the prostate.<sup>63,69</sup>

#### 4.3 | Metabolite tissue concentrations

Our estimated tissue concentrations for tCho, tCr, Spm, and mI agree well with reports of 2.6 to 7 mM for tCho, 4 to

9 mM for tCr, 7 to 13 mM for Spm, and 10 and 18 mM for mI as measured by *in vivo*  $^1\text{H}$ -MRS of the prostate.<sup>36-38,41,43,70</sup> The average tissue concentration for Cit aligns well with *in vivo* MRS studies of Cit in the TZ, reporting values between ~20 and 40 mM,<sup>38,43,47,71,72</sup> in agreement with the dominant contribution of the TZ to the selected VOI for the DW-MRS examinations.

Are the tissue concentrations of Cit, Spm, and mI in agreement with a nearly complete luminal origin of these compounds taking into account their concentrations in EPF and assuming this represents luminal fluid? Average Cit concentrations in EPF have been estimated to be ~90 mM by enzymatic analysis<sup>49,73</sup> and up to ~350 mM by NMR.<sup>22,23</sup> With an average luminal volume fraction of the prostate of 25% this translates to an *in vivo* tissue concentration range of 23 to 88 mM, which matches with the range of Cit concentrations found *in vivo* by MRS for the TZ and the PZ in normal prostates.<sup>20,38,43,47,71,72</sup> Considering that the estimated Cit concentration in epithelial cells is ~1 mM,<sup>73</sup> this indicates that its signal in  $^1\text{H}$ -MR spectra nearly completely stems from the luminal space. In EPF of healthy subjects, average Spm concentrations of 44 and 58 mM have been measured by NMR.<sup>21,23</sup> Again, taking a 25% luminal volume fraction into account this translates to *in vivo* tissue concentrations of 12 to 15 mM, which is close to the tissue concentrations measured by *in vivo* MRS,<sup>37,38,43</sup> therefore, indicating that also the signal of Spm largely comes from the lumen. Average mI concentrations in EPF of ~21 and 27 mM have been reported,<sup>21,23</sup> which would represent tissue concentrations of 5 to 7 mM with 25% luminal volume. As this is lower than the tissue concentrations estimated by *in vivo*  $^1\text{H}$ -MRS and by our DW-MRS study it remains unclear to which extent the signal of mI comes from the luminal space or has a cellular origin.<sup>23</sup>

If the biexponential signal decay of water would yield an unambiguous estimate for the luminal volume fraction, this could be used to derive luminal-specific Cit and Spm contents. Given the likely contribution of the stromal signal to both diffusion components, this is not possible with the current limited *b*-value data. Combining diffusion and relaxometry seems a more promising approach.<sup>13,14</sup>

#### 4.4 | Supporting *in vitro* information

The levels of Cit and Spm in EPF are closely associated<sup>21,23</sup> and recently we provided evidence from changes in  $T_2$  relaxation that these metabolites interact with each other in solutions approaching EPF compositions.<sup>50</sup> In the current study, we determined the diffusion properties of Cit, Spm, and mI in similar solutions and observed slowdown in Spm diffusion with increasing Cit content and vice

versa confirming the formation of a (transient) Cit-Spm complex, partly explaining reduced ADC values for both molecules *in vivo* with respect to the freely diffusing compounds. In normal prostatic fluid, Cit has a ~5 times higher concentration than Spm, such that a 1:1 Cit-Spm complex would not deplete the free Cit pool. This explains the higher ADC for Cit in the EPF mimic, which is in line with a much larger  $T_2$  decrease of Spm compared to Cit when mixing these two at a 5:1 ratio.<sup>50</sup> The ratio of the ADCs of Cit and Spm is ~1 for the individually dissolved compounds, ~1.2 for the EPF mimic, and ~1.4 *in vivo* suggesting a free Cit fraction higher than that of Spm in the luminal space of the prostate.  $T_2$  relaxation studies indicate that the formation of a Cit-Spm complex is promoted by cations, in particular  $\text{Zn}^{2+}$ .<sup>50</sup>

Prostatic fluid contains many proteins of which serum albumin is one of the dominant ones.<sup>74,75</sup> We have taken 15 g/L BSA as a surrogate representing the average total protein content of normal EPF.<sup>75</sup> Adding 15 g/L BSA to the solutions decreased the ADC of all three metabolites and that of water, but mostly of mI. Increasing BSA to 50 g/L had no further effect on the ADCs, except for that of mI, which substantially decreased even further. Remarkably, in the presence of ions, BSA has no effect on the  $T_2$  of mI.<sup>50</sup>

The ADCs of Cit, Spm, and mI in this final EPF mimic solution were still well above the ADCs of these compounds measured *in vivo*. This implies that *in vivo* they are involved in further interactions such as with proteins or macromolecules or in higher-order complexes, or they are hindered by increased viscosity or undiscovered diffusion barriers within prostatic fluid. For instance, the average concentration of  $\text{Zn}^{2+}$  in EPF of healthy volunteers can reach ~10 mM<sup>76</sup>; higher than the 4 mM applied in our study. A concentration of 9 mM substantially further decreased the  $T_2$  values of the compounds<sup>50</sup> and could also affect ADC values. The luminal space in the prostate may contain large molecular complexes such as corpora amylacea, commonly associated with prostate inflammation,<sup>77</sup> which could have a profound effect on molecular diffusion. Although mI is found in high concentrations in EPF,<sup>21,23</sup> an as yet unknown fraction may reside in prostate cells, causing more restricted diffusion of the molecule.

#### 4.5 | Limitations and future options

We mitigated effects of motion and susceptibility changes on spectral quality by volunteer preparation and specific postprocessing procedures (*vide supra*). This helped considerably, but residual effects from inconsistent data over the whole time course of the measurements cannot be excluded.

More *b*-values could help extracting multiple diffusion decays for water and metabolites residing in multiple environments. Additionally, multi-directional diffusion weighting could reveal anisotropic microstructures.

A limitation of this study was the selection of a single relatively large voxel, which covered both PZ and TZ tissue of the prostate. A multivoxel approach or smaller voxels that more specifically target more homogeneous tissue or focal lesions would be desirable, but this obviously requires better SNR (e.g., using higher magnetic fields).

## 5 | CONCLUSIONS

This study presents a pioneering investigation of <sup>1</sup>H-DW-MRS in the prostate, overcoming challenges such as motion artifacts and limited SNR. By co-acquiring a water signal for corrections and implementing a motion-compensation scheme, we successfully addressed inter-acquisition distortions, phase and frequency fluctuations, eddy-current distortions, and nonlinear motion. Simultaneous fitting of spectra and DW signal attenuation further improved the accuracy and precision of our findings. The measured ADCs for prostate metabolites demonstrate the feasibility of <sup>1</sup>H-DW-MRS in the prostate to study effects of the micro-environment and metabolite complexation on these ADCs. Discrepancies between ADC values found in vivo and in vitro for luminal metabolites need further investigation. The application of <sup>1</sup>H-DW-MRS may improve our understanding of the biology of the healthy and diseased prostate.

## ACKNOWLEDGMENTS







We thank Roger Bourne and Aritrick Chatterjee for valuable discussions. In addition, we acknowledge that as a result of a multi-institution collaboration with distributed know-how, Arend Heerschap, Tom Scheenen, and Roland Kreis contributed equally as last authors to this work. This project has received funding from the European Union's Horizon 2020 research and innovation program under the Marie Skłodowska-Curie grant agreement 813120. Open access funding provided by Universitat Bern.

## FUNDING INFORMATION

European Union's Horizon 2020 research and innovation program under the Marie Skłodowska-Curie, Grant Agreement: 813120.

## ORCID

Angeliki Stamatelatou  <https://orcid.org/0000-0002-3956-8731>

Rudy Rizzo  <https://orcid.org/0000-0003-4572-5120>  
 Kadir Simsek  <https://orcid.org/0000-0003-4044-7395>  
 Jack J A van Asten  <https://orcid.org/0000-0002-2135-5682>  
 Arend Heerschap  <https://orcid.org/0000-0001-9930-4562>  
 Tom Scheenen  <https://orcid.org/0000-0002-4468-1480>  
 Roland Kreis  <https://orcid.org/0000-0002-8618-6875>

## REFERENCES

- Packer JR, Maitland NJ. The molecular and cellular origin of human prostate cancer. *Biochim Biophys Acta – Mol. Cell Res.* 2016;1863:1238-1260. doi:10.1016/j.bbamcr.2016.02.016
- Verze P, Cai T, Lorenzetti S. The role of the prostate in male fertility, health and disease. *Nat Rev Urol.* 2016;13:379-386. doi:10.1038/nrurol.2016.89
- McNeal JE. Normal histology of the prostate. *Am J Surg Pathol.* 1988;12:619-633. doi:10.1097/0000478-198808000-00003
- Padhani AR, Barentsz J, Villeirs G, et al. PI-RADS steering committee: the PI-RADS multiparametric MRI and MRI-directed biopsy pathway. *Radiology.* 2019;292:464-474. doi:10.1148/radiol.2019182946
- Maurer MH, Heverhagen JT. Diffusion weighted imaging of the prostate-principles, application, and advances. *Transl Androl Urol.* 2017;6:490-498. doi:10.21037/tau.2017.05.06
- Kobus T, Vos PC, Hambrock T, et al. Prostate cancer aggressiveness: in vivo assessment of MR spectroscopy and diffusion-weighted imaging at 3 T. *Radiology.* 2012;265:457-467. doi:10.1148/radiol.12111744
- Fennessy FM, Maier SE. Quantitative diffusion MRI in prostate cancer: image quality, what we can measure and how it improves clinical assessment. *Eur J Radiol.* 2023;167:111066. doi:10.1016/J.EJRAD.2023.111066
- Bourne RM, Kurniawan N, Cowin G, et al. Microscopic diffusivity compartmentation in formalin-fixed prostate tissue. *Magn Reson Med.* 2012;68:614-620. doi:10.1002/mrm.23244
- Sabouri S, Fazli L, Chang SD, et al. MR measurement of luminal water in prostate gland: quantitative correlation between MRI and histology. *J Magn Reson Imaging.* 2017;46:861-869. doi:10.1002/jmri.25624
- Panagiotaki E, Chan RW, Dikaios N, et al. Microstructural characterization of normal and malignant human prostate tissue with vascular, extracellular, and restricted diffusion for cytometry in tumours magnetic resonance imaging. *Invest Radiol.* 2015;50:218-227. doi:10.1097/RLI.000000000000115
- Yamin G, Schenker-Ahmed NM, Shabaik A, et al. Voxel level radiologic-pathologic validation of restriction spectrum imaging cellularity index with gleason grade in prostate cancer. *Clin Cancer Res.* 2016;22:2668-2674. doi:10.1158/1078-0432.CCR-15-2429
- Chatterjee A, Bourne RM, Wang S, et al. Diagnosis of prostate cancer with noninvasive estimation of prostate tissue composition by using hybrid multidimensional MR imaging: a feasibility study. *Radiology.* 2018;287:864-873. doi:10.1148/radiol.2018171130
- Chatterjee A, Mercado C, Bourne RM, et al. Validation of prostate tissue composition by using hybrid multidimensional MRI: correlation with histologic findings. *Radiology.* 2022;302:368-377. doi:10.1148/radiol.2021204459

14. Palombo M, Valindria V, Singh S, et al. Joint estimation of relaxation and diffusion tissue parameters for prostate cancer with relaxation-VERDICT MRI. *Sci Rep.* 2023;13:2999. doi:10.1038/s41598-023-30182-1
15. Selnæs KM, Heerschap A, Jensen LR, et al. Peripheral zone prostate cancer localization by multiparametric magnetic resonance at 3T: unbiased cancer identification by matching to histopathology. *Invest Radiol.* 2012;47:624-633. doi:10.1097/RLI.0b013e318263f0fd
16. Palombo M, Shemesh N, Ronen I, Valette J. Insights into brain microstructure from in vivo DW-MRS. *Neuroimage.* 2018;182:116. doi:10.1016/j.neuroimage.2017.11.028
17. Ronen I, Valette J. Diffusion-weighted magnetic resonance spectroscopy. *EMagRes.* 2015;4:4. doi:10.1002/9780470034590.emrstm1471
18. Brandejsky V, Boesch C, Kreis R. Proton diffusion tensor spectroscopy of metabolites in human muscle in vivo. *Magn Reson Med.* 2015;73:481-487. doi:10.1002/mrm.25139
19. Ligneul C, Najac C, Döring A, et al. Diffusion-weighted MR spectroscopy: consensus, recommendations, and resources from acquisition to modeling. *Magn Reson Med.* 2024;91:860-885. doi:10.1002/mrm.29877
20. Stamatelatos A, Scheenen TWJ, Heerschap A. Developments in proton MR spectroscopic imaging of prostate cancer. *Magn Reson Med.* 2022;35:645-665. doi:10.1007/s10334-022-01011-9
21. Lynch MJ, Nicholson JK. Proton MRS of human prostatic fluid: correlations between citrate, spermine, and myo-inositol levels and changes with disease. *Prostate.* 1997;30:248-255. doi:10.1002/(SICI)1097-0045(19970301)30:4<248::AID-PROSA>3.0.CO;2-H
22. Kline EE, Treat EG, Averna TA, Davis MS, Smith AY, Sillerud LO. Citrate concentrations in human seminal fluid and expressed prostatic fluid determined via 1H nuclear magnetic resonance spectroscopy outperform prostate specific antigen in prostate cancer detection. *J Urol.* 2006;176:2274-2279. doi:10.1016/j.juro.2006.07.054
23. Serkova NJ, Gamito EJ, Jones RH, et al. The metabolites citrate, myo-inositol, and spermine are potential age-independent markers of prostate cancer in human expressed prostatic secretions. *Prostate.* 2008;68:620-628. doi:10.1002/pros.20727
24. Park S, Ang RR, Duffy SP, et al. Morphological differences between circulating tumor cells from prostate cancer patients and cultured prostate cancer cells. *PLoS One.* 2014;9:e85264. doi:10.1371/journal.pone.0085264
25. Bailey C, Bourne RM, Siow B, et al. VERDICT MRI validation in fresh and fixed prostate specimens using patient-specific moulds for histological and MR alignment. *NMR Biomed.* 2019;32:e4073. doi:10.1002/nbm.4073
26. Iczkowski KA, Torkko KC, Kotnis GR, et al. Pseudolumen size and perimeter in prostate cancer: correlation with patient outcome. *Prostate Cancer.* 2011;2011:69385. doi:10.1155/2011/693853
27. Dreher W, Leibfritz D. New method for the simultaneous detection of metabolites and water in localized in vivo 1H nuclear magnetic resonance spectroscopy. *Magn Reson Med.* 2005;54:190-195. doi:10.1002/mrm.20549
28. Döring A, Adalid V, Boesch C, Kreis R. Diffusion-weighted magnetic resonance spectroscopy boosted by simultaneously acquired water reference signals. *Magn Reson Med.* 2018;80:2326-2338. doi:10.1002/mrm.27222
29. Şimşek K, Döring A, Pampel A, Möller HE, Kreis R. Macromolecular background signal and non-gaussian metabolite diffusion determined in human brain using ultra-high diffusion weighting. *Magn Reson Med.* 2022;88:1962-1977. doi:10.1002/mrm.29367
30. Chong DGQ, Kreis R, Bolliger CS, Boesch C, Slotboom J. Two-dimensional linear-combination model fitting of magnetic resonance spectra to define the macromolecule baseline using FiTAID, a fitting tool for arrays of interrelated datasets. *MAGMA.* 2011;24:147-164. doi:10.1007/s10334-011-0246-y
31. Adalid V, Döring A, Kyathanahally SP, Bolliger CS, Boesch C, Kreis R. Fitting interrelated datasets: metabolite diffusion and general lineshapes. *MAGMA.* 2017;30:429-448. doi:10.1007/s10334-017-0618-z
32. Frahm J, Merboldt KD, Hänicke W. Localized proton spectroscopy using stimulated echoes. *J Magn Reson.* 1987;72:502-508. doi:10.1016/0022-2364(87)90154-5
33. Brandejsky V, Kreis R, Boesch C. Restricted or severely hindered diffusion of intramyocellular lipids in human skeletal muscle shown by in vivo proton MR spectroscopy. *Magn Reson Med.* 2012;67:310-316. doi:10.1002/mrm.23024
34. Soher BJ, Semanchuk P, Todd D, Steinberg J, Young K. VeSPA: integrated applications for RF pulse design, spectral simulation and MRS data analysis. *Magn Reson Med.* 2023;90:823-838. doi:10.1002/mrm.29686
35. Scheenen TWJ, Gambarota G, Weiland E, et al. Optimal timing for in vivo 1H-MR spectroscopic imaging of the human prostate at 3T. *Magn Reson Med.* 2005;53:1268-1274. doi:10.1002/mrm.20468
36. Weis J, Ortiz-Nieto F, Ahlström H. MR spectroscopy of the prostate at 3T: measurements of relaxation times and quantification of prostate metabolites using water as an internal reference. *Magn Reson Med Sci.* 2013;12:289-296. doi:10.2463/mrms.2013-0017
37. Basharat M, Payne GS, Morgan VA, Parker C, Dearnaley D, de Souza NM. TE = 32 ms vs TE = 100 ms echo-time 1H-magnetic resonance spectroscopy in prostate cancer: tumor metabolite depiction and absolute concentrations in tumors and adjacent tissues. *J Magn Reson Imaging.* 2015;42:1086-1093. doi:10.1002/jmri.24875
38. Basharat M, Jafar M, de Souza NM, Payne GS. Evaluation of short-TE 1H MRSI for quantification of metabolites in the prostate. *NMR Biomed.* 2014;27:467. doi:10.1002/nbm.3082
39. Le Bihan D, Breton E, Lallemand D, Aubin ML, Vignaud J, Laval-Jeantet M. Separation of diffusion and perfusion in intravoxel incoherent motion MR imaging. *Radiology.* 1988;168:497-505. doi:10.1148/radiology.168.2.3393671
40. Shen L, Zhou L, Liu X, Yang X. Comparison of biexponential and monoexponential DWI in evaluation of Fuhrman grading of clear cell renal cell carcinoma. *Diagn Interv Radiol.* 2017;23:100-105. doi:10.5152/dir.2016.15519
41. Tayari N, Wright AJ, Heerschap A. Absolute choline tissue concentration mapping for prostate cancer localization and characterization using 3D 1H MRSI without water-signal suppression. *Magn Reson Med.* 2022;87:561-573. doi:10.1002/mrm.29012
42. Tayari N, Heerschap A, Scheenen TWJ, Kobus T. In vivo MR spectroscopic imaging of the prostate, from application to interpretation. *Anal Biochem.* 2017;529:170. doi:10.1016/j.ab.2017.02.001

43. Weis J, von Below C, Tolf A, et al. Quantification of metabolite concentrations in benign and malignant prostate tissues using 3D proton MR spectroscopic imaging. *J Magn Reson Imaging*. 2017;45:1232-1240. doi:10.1002/jmri.25443
44. Gibbs P, Liney GP, Pickles MD, Zelhof B, Rodrigues G, Turnbull LW. Correlation of ADC and T<sup>2</sup> measurements with cell density in prostate cancer at 3.0 tesla. *Invest Radiol*. 2009;44:572-576. doi:10.1097/rli.0b013e3181b4c10e
45. De Bazelaire CMJ, Duhamel GD, Rofsky NM, Alsop DC. MR imaging relaxation times of abdominal and pelvic tissues measured in vivo at 3.0 T: preliminary results. *Radiology*. 2004;230:652-659. doi:10.1148/radiol.2303021331
46. Baur ADJ, Hansen CM, Rogasch J, et al. Evaluation of T<sup>1</sup> relaxation time in prostate cancer and benign prostate tissue using a modified look-locker inversion recovery sequence. *Sci Rep*. 2020;10:3121. doi:10.1038/s41598-020-59942-z
47. Lowry M, Liney GP, Turnbull LW, Manton DJ, Blackband SJ, Horsman A. Quantification of citrate concentration in the prostate by proton magnetic resonance spectroscopy: zonal and age-related differences. *Magn Reson Med*. 1996;36:352-358. doi:10.1002/mrm.1910360305
48. Hamilton EI. Report of the task group on reference man, international commission on radiological protection publication 23. *Sci Total Environ*. 1976;6:201-202. doi:10.1016/0048-9697(76)90016-4
49. Kavanagh JP. Sodium, potassium, calcium, magnesium, zinc, citrate and chloride content of human prostatic and seminal fluid. *J Reprod Fertil*. 1985;75:35-41. doi:10.1530/jrf.0.0750035
50. Jupin M, van Heijster FHA, Heerschap A. Metabolite interactions in prostatic fluid mimics assessed by 1H NMR. *MAGMA*. 2022;35:683-694. doi:10.1007/s10334-021-00983-4
51. Rydhög AS, Szczepankiewicz F, Wirestam R, et al. Separating blood and water: perfusion and free water elimination from diffusion MRI in the human brain. *Neuroimage*. 2017;156:434. doi:10.1016/j.neuroimage.2017.04.023
52. Le BD. Molecular diffusion, tissue microdynamics and microstructure. *NMR Biomed*. 1995;8:375-386. doi:10.1002/nbm.1940080711
53. Sprenger CC, Plymate SR, Reed MJ. Aging-related alterations in the extracellular matrix modulate the microenvironment and influence tumor progression. *Int J Cancer*. 2010;127:2739-2748. doi:10.1002/ijc.25615
54. Bissell MJ, Radisky D. Putting tumours in context. *Nat Rev Cancer*. 2001;1:46-54. doi:10.1038/35094059
55. Guneyli S, Ward E, Thomas S, et al. Magnetic resonance imaging of benign prostatic hyperplasia. *Diagnostic Interv Radiol*. 2016;22:215-219. doi:10.5152/dir.2015.15361
56. Langer DL, van der Kwast TH, Evans AJ, et al. Prostate tissue composition and MR measurements: investigating the relationships between ADC, T<sup>2</sup>, Ktrans, Ve, and corresponding histologic features. *Radiology*. 2010;255:485-494. doi:10.1148/radiol.10091343
57. Chatterjee A, Watson G, Myint E, Sved P, McEntee M, Bourne R. Changes in epithelium, stroma, and lumen space correlate more strongly with gleason pattern and are stronger predictors of prostate ADC changes than cellularity metrics. *Radiology*. 2015;277:751-762. doi:10.1148/radiol.2015142414
58. Shiradkar R, Panda A, Leo P, et al. T<sup>1</sup> and T<sup>2</sup> MR fingerprinting measurements of prostate cancer and prostatitis correlate with deep learning-derived estimates of epithelium, lumen, and stromal composition on corresponding whole mount histopathology. *Eur Radiol*. 2021;31:1336-1346. doi:10.1007/s00330-020-07214-9
59. Chan RW, Lau AZ, Detzler G, Thayalasuthan V, Nam RK, Haider MA. Evaluating the accuracy of multicomponent T<sup>2</sup> parameters for luminal water imaging of the prostate with acceleration using inner-volume 3D GRASE. *Magn Reson Med*. 2019;81:466-476. doi:10.1002/mrm.27372
60. Zhang Z, Wu HH, Priester A, et al. Prostate microstructure in prostate cancer using 3-T MRI with diffusion-relaxation correlation Spectrum imaging: validation with whole-mount digital histopathology. *Radiology*. 2020;296:348-355. doi:10.1148/radiol.2020192330
61. Kobus T, van der Laak JAWM, Maas MC, et al. Contribution of histopathologic tissue composition to quantitative MR spectroscopy and diffusion-weighted imaging of the prostate. *Radiology*. 2016;278:811. doi:10.1148/radiol.2015142889
62. Babinski MA, Chagas MA, Costa WS, Sampaio FJ. Prostatic epithelial and luminal area in the transition zone acini: morphometric analysis in normal and hyperplastic human prostate. *BJU Int*. 2003;92:592-596. doi:10.1046/j.1464-410X.2003.04433.x
63. Mulkern RV, Barnes AS, Haker SJ, et al. Biexponential characterization of prostate tissue water diffusion decay curves over an extended b-factor range. *Magn Reson Imaging*. 2006;24:563-568. doi:10.1016/j.mri.2005.12.008
64. Shinmoto H, Oshio K, Tanimoto A, et al. Biexponential apparent diffusion coefficients in prostate cancer. *Magn Reson Imaging*. 2009;27:355-359. doi:10.1016/J.MRI.2008.07.008
65. Bourne RM, Kurniawan N, Cowin G, et al. Biexponential diffusion decay in formalin-fixed prostate tissue: preliminary findings. *Magn Reson Med*. 2012;68:954-959. doi:10.1002/mrm.23291
66. Najac C, Branzoli F, Ronen I, Valette J. Brain intracellular metabolites are freely diffusing along cell fibers in grey and white matter, as measured by diffusion-weighted MR spectroscopy in the human brain at 7 T. *Brain Struct Funct*. 2016;221:1245-1254. doi:10.1007/s00429-014-0968-5
67. Ingo C, Brink W, Ercan E, Webb AG, Ronen I. Studying neurons and glia non-invasively via anomalous subdiffusion of intracellular metabolites. *Brain Struct Funct*. 2018;223:3841-3854. doi:10.1007/s00429-018-1719-9
68. Döring A, Kreis R. Magnetic resonance spectroscopy extended by oscillating diffusion gradients: cell-specific anomalous diffusion as a probe for tissue microstructure in human brain. *Neuroimage*. 2019;202:116075. doi:10.1016/j.neuroimage.2019.116075
69. Mazaheri Y, Hötker AM, Shukla-Dave A, Akin O, Hricak H. Model selection for high b-value diffusion-weighted MRI of the prostate. *Magn Reson Imaging*. 2018;46:27. doi:10.1016/j.mri.2017.10.003
70. Heerschap A, Jager GJ, Van Der Graaf M, Barentsz JO, Ruijs SHJ. Proton MR spectroscopy of the normal human prostate with an endorectal coil and a double spin-echo pulse sequence. *Magn Reson Med*. 1997;37:204-213. doi:10.1002/mrm.1910370212
71. Stamatelatos A, Sima DM, van Huffel S, van Asten JJA, Heerschap A, Scheenen TWJ. Post-acquisition water-signal removal in 3D water-unsuppressed 1H-MR spectroscopic imaging of the prostate. *Magn Reson Med*. 2023;89:1741-1753. doi:10.1002/mrm.29565

72. Swanson MG, Zektzer AS, Tabatabai ZL, et al. Quantitative analysis of prostate metabolites using 1H HR-MAS spectroscopy. *Magn Reson Med.* 2006;55:1257-1264. doi:10.1002/mrm.20909
73. Costello LC, Franklin RB. Concepts of citrate production and secretion by prostate 1. Metabolic relationships. *Prostate.* 1991;18:25-46. doi:10.1002/pros.2990180104
74. Drake RR, White KY, Fuller TW, et al. Clinical collection and protein properties of expressed prostatic secretions as a source for biomarkers of prostatic disease. *J Proteomics.* 2009;72:907-917. doi:10.1016/j.jprot.2009.01.007
75. Gann PH, Chatterton R, Vogelsong K, Grayhack JT, Lee C. Epidermal growth factor-related peptides in human prostatic fluid: sources of variability in assay results. *Prostate.* 1997;32:234-240. doi:10.1002/(SICI)1097-0045(19970901)32:4<234::AID-PROS2>3.0.CO;2-J
76. Zaichick VY, Sviridova TV, Zaichick SV. Zinc concentration in human prostatic fluid: Normal, chronic prostatitis, adenoma and cancer. *Int Urol Nephrol.* 1996;28:687-694. doi:10.1007/BF02552165
77. DuPre NC, Flavin R, Sfanos KS, et al. Corpora amylacea in prostatectomy tissue and associations with molecular, histological, and lifestyle factors. *Prostate.* 2018;78:1172-1180. doi:10.1002/pros.23692

**How to cite this article:** Stamatelatou A, Rizzo R, Simsek K, et al. Diffusion-weighted MR spectroscopy of the prostate. *Magn Reson Med.* 2024;1-15. doi: 10.1002/mrm.30141